HHS Public Access

Author manuscript

Adv Funct Mater. Author manuscript; available in PMC 2021 January 23.

Published in final edited form as:

Adv Funct Mater. 2020 January 23; 30(4): . doi:10.1002/adfm.201907716.

In Situ Polymerized Hollow Mesoporous Organosilica Biocatalysis Nanoreactor for Enhancing ROS-Mediated Anticancer Therapy

Ling Li[†],

Department of PET Center, National Clinical Research Center for Geriatric Disorders, Xiangya Hospital,Central South University, Changsha 410008, China

Laboratory of Molecular Imaging and Nanomedicine (LOMIN), National Institute of Biomedical Imaging and Bioengineering (NIBIB), National Institutes of Health (NIH), Bethesda, Maryland 20892, United States

Zhen Yang[†],

Laboratory of Molecular Imaging and Nanomedicine (LOMIN), National Institute of Biomedical Imaging and Bioengineering (NIBIB), National Institutes of Health (NIH), Bethesda, Maryland 20892, United States

Wenpei Fan,

Laboratory of Molecular Imaging and Nanomedicine (LOMIN), National Institute of Biomedical Imaging and Bioengineering (NIBIB), National Institutes of Health (NIH), Bethesda, Maryland 20892, United States

Liangcan He,

Laboratory of Molecular Imaging and Nanomedicine (LOMIN), National Institute of Biomedical Imaging and Bioengineering (NIBIB), National Institutes of Health (NIH), Bethesda, Maryland 20892, United States

Cao Cui,

Department of Orthopedics, Xiangyang Central Hospital, Affiliated Hospital of Hubei University of Arts and Science, Xiangyang, Hubei 441021, China

Jianhua Zou,

Laboratory of Molecular Imaging and Nanomedicine (LOMIN), National Institute of Biomedical Imaging and Bioengineering (NIBIB), National Institutes of Health (NIH), Bethesda, Maryland 20892, United States

Wei Tang,

Laboratory of Molecular Imaging and Nanomedicine (LOMIN), National Institute of Biomedical Imaging and Bioengineering (NIBIB), National Institutes of Health (NIH), Bethesda, Maryland 20892, United States

hushuoxy@csu.edu.cn.

[†]L. Li and Z. Yang contributed equally to this work

Supporting Information

Supporting Information is available from the Wiley Online Library or from the author.

Orit Jacobson,
Laboratory of Molecular Imaging and Nanomedicine (LOMIN), National Institute of Biomedical Imaging and Bioengineering (NIBIB), National Institutes of Health (NIH), Bethesda, Maryland 20892, United States

Zhantong Wang,
Laboratory of Molecular Imaging and Nanomedicine (LOMIN), National Institute of Biomedical Imaging and Bioengineering (NIBIB), National Institutes of Health (NIH), Bethesda, Maryland 20892, United States

Gang Niu,
Laboratory of Molecular Imaging and Nanomedicine (LOMIN), National Institute of Biomedical Imaging and Bioengineering (NIBIB), National Institutes of Health (NIH), Bethesda, Maryland 20892, United States

Shuo Hu,
Department of PET Center, National Clinical Research Center for Geriatric Disorders, Xiangya Hospital,Central South University, Changsha 410008, China

Xiaoyuan Chen
Laboratory of Molecular Imaging and Nanomedicine (LOMIN), National Institute of Biomedical Imaging and Bioengineering (NIBIB), National Institutes of Health (NIH), Bethesda, Maryland 20892, United States

Abstract

The combination of reactive oxygen species (ROS)-involved photodynamic therapy (PDT) and chemodynamic therapy (CDT) holds great promise for enhancing ROS-mediated cancer treatment. Herein, we reported an *in situ* polymerized hollow mesoporous organosilica nanoparticle (HMON) biocatalysis nanoreactor to integrate the synergistic effect of PDT/CDT for enhancing ROS-mediated pancreatic ductal adenocarcinoma treatment. HPPH photosensitizer was hybridized within the framework of HMON *via* an "*in situ* framework growth" approach. Then, the hollow cavity of HMONs was exploited as a nanoreactor for "*in situ* polymerization" to synthesize the polymer containing thiol groups, thereby enabling the immobilization of ultrasmall gold nanoparticles, which behave like glucose oxidase-like nanozyme, converting glucose into H_2O_2 to provide self-supplied H_2O_2 for CDT. Meanwhile, Cu^{2+}-tannic acid complexes were further deposited on the surface of HMONs (HMON-Au@Cu-TA) to initiate Fenton-like reaction to covert the self-supplied H_2O_2 into •OH, a highly toxic ROS. Finally, collagenase (Col), which can degrade the collagen I fiber in the extracellular matrix (ECM), was loaded into HMON-Au@Cu-TA to enhance the penetration of HMONs and O_2 infiltration for enhanced PDT. This study provides a good paradigm for enhancing ROS-mediated anti-tumor efficacy. Meanwhile, this research offers a new method to broaden the application of silica based nanotheranostics.

Keywords

mesoporous organosilica; *in situ* polymerization; ultra-small gold nanoparticle; Fenton-like reaction; chemodynamic therapy

1. Introduction

In the past decades, photodynamic therapy (PDT), which uses non-toxic photosensitizers and harmless visible/near infrared light in combination with oxygen (O_2) to produce cytotoxic reactive oxygen species (ROS), has been intensively applied to cancer therapy due to its minimal systemic toxicity and reduced side effects.[1] In most cases, however, the therapeutic benefit of PDT is largely limited, owing to the low ROS generation efficiency in the hypoxic tumor micro-environment (TME) and light attenuation.[2] Meanwhile, tumors have also evolved many mechanisms to balance oxidative damage to protect tumor cells from death.[3] Thus, effective cancer treatment requires a relatively high level of ROS to induce irreversible oxidative damage to tumor cells. In recent years, chemodynamic therapy (CDT) has attracted much attention due to its high efficiency and minimal side effects.[4] CDT employs Fenton or Fenton-like reactions to convert hydrogen peroxide (H_2O_2) into oxidative hydroxyl radicals (•OH), one of the most toxic ROS.[5] In CDT, tumor site-specific endogenous chemical energy was exploited to produce •OH, thus preventing normal tissues to oxidative damage. In contrast to PDT, CDT is independent of the local oxygen concentration. Meanwhile, endogenous chemical stimuli rather than external energy input was used to initiate PDT, thereby avoiding the quick energy attenuation. Unfortunately, although the H_2O_2 level in TME is relatively high compared to the normal tissues, the amount of endogenous H_2O_2 is still insufficient to achieve effective CDT.[6] We speculate that *in situ* generation of H_2O_2 to increase the efficacy of Fenton-like reaction in TME could be a promising strategy to achieve enhanced CDT.

Nanozymes, nanomaterial-based artificial enzymes, have attracted significant attention owing to its striking merits.[7] In comparison to natural enzymes, nanozymes have a number of advantages, such as low expense and ability to recycle, ease of manufacturing, and high catalytic stability.[8] More importantly, nanozymes can work in environments closer to physiological conditions and can be designed with a range of catalytic activity by simply varying shape, structure, and composition based on their size/composition dependent activity. Typically, the ultra-small (< 3.6 nm) gold nanoparticle (Au NPs), a glucose oxidase-like nanozyme, can catalyze glucose into H_2O_2 and gluconic acid with high efficiency.[9] However, due to the addition of large amounts of surfactants to stabilize the ultra-small Au NPs during preparation, the ultra-small Au NPs cannot be used for biomedical applications directly. Meanwhile, such small-sized Au NPs can be rapidly cleared from the systemic circulation through the kidney.[10] Thus, a desirable nanocarrier to immobilize the ultra-small Au NPs is necessary to ensure their biosafety and catalytic effect *in vivo*. Hollow mesoporous organosilica nanoparticles (HMONs) have been widely employed as drug/gene delivery systems due to its excellent loading capacity, biocompatibility and biodegradability.[11] Most importantly, owing to the hollow mesoporous structure, HMONs would not block the entry and exit of substances, such as the catalytic substrates and the catalytic products, which is critical for successful catalysis. Thus, we assume that HMONs could be an appropriate candidate nanocarrier for immobilizing the ultra-small Au NPs.

Typically, several kinds of metal ions, such as Fe^{2+}, Cu^{2+}, Mn^{2+} and Co^{2+}, have shown excellent Fenton-like catalytic activity. In general, these metal ions cannot be applied directly due to their potential systemic toxicity. Tannic acid (TA), one of the most abundant

polyphenols in plants, has been accepted by FDA with wide application in food and medicine. The digalloyl groups rich in TA can serve as chelating sites for multivalent metal ions.[12] Meanwhile, metal-TA complexes exhibit pH-disassembly kinetics. At low pH, hydroxyl groups of TA are protonated, leading to destabilization of cross-links between metal ions and TA.[13] Additionally, some reports have demonstrated that TA can deposit on the surface of the HMONs by surface interactions.[14]

Herein, we described an "*in situ* framework growth" approach to construct HMONs hybridized with the photosensitizer, 2-(1-hexyloxyethyl)-2-devinylpyropheophorbide-a (HPPH), through co-hydrolysis of HPPH-silane and organosilane/inorganosilane precursors during the synthesis (Scheme 1). HPPH, a second-generation chlorin-based photosensitizer, has shown favorable photophysical and pharmacokinetic properties in preclinical studies. Currently, it has confirmed its effectiveness in early or late-stage lung cancer and esophageal cancer patients.[15] This *in situ* growth of HPPH within the framework would not block the mesopores of HMONs, thus facilitating the drug loading, and the entry and exit of substances. More importantly, for the first time, the hollow cavity of HMONs was exploited as a nanoreactor for "*in situ* polymerization" to synthesize the polymer containing thiol groups, thereby enabling the immobilization of ultra-small Au nanoparticles to covert glucose into H_2O_2. Distinct from the previous report which performed *in situ* polymerization in the pores of the mesoporous silica nanoparticles,[16] owing to the restriction of the shell of HMONs, the resulting polymer containing thiol groups in our study can be trapped in the hollow cavity to immobilize the Au NPs *via* the chelation effect. Then, TA was deposited on the surface of the HMONs to initiate the coordination with the metal ions, Cu^{2+}, to trigger Fenton-like reaction. Furthermore, to enhance the penetration of HMONs and O_2 infiltration, collagenase (Col), which can degrade the collagen I fiber in the extracellular matrix (ECM), was loaded into HMONs nanocarrier based on the interaction with Cu-TA complexes. Finally, the prepared HMONs were coated with Polyvinylpyrrolidone (PVP) to enable high physiological stability during systemic circulation when used *in vivo*.

2. Results and Discussion

2.1. Preparation and characterization of *in situ* polymerized hollow mesoporous organosilica biocatalysis nanoreactor

To begin, an "*in situ* framework growth" approach was applied to prepare HPPH hybridized HMONs. In brief, HPPH was first conjugated with (3-aminopropyl) triethoxysilane (APTES) *via* amidation reaction (Figure S1, Supporting Information). Then HPPH hybridized HMONs were prepared through co-hydrolysis with other silica precursors. UV-Vis spectra showed that after hybridized within the framework of HMONs, HPPH exhibited a slightly red-shifted absorption peak (Figure 1a). The fluorescence emission spectrum of HPPH hybridized HMONs indicated that HPPH was well dispersed in HMON (Figure 1b). To examine whether hybridization within the framework of HMONs could influence the photodynamic effect of HPPH, the Singlet Oxygen Sensor Green (SOSG) fluorescence probe was used to detect the singlet oxygen ($^1O_2$) generation capability of HPPH hybridized HMONs. As displayed in Figure 1c, hybridization within the framework of HMONs retained the $^1O_2$ generation capability of HPPH (Figure S2, Supporting Information). The prepared

HMON was ~ 40 nm in diameter, as measured by transmission electron microscopy (TEM, JEOL TEM 2010 electron microscope) (Figure 1d and Figure S3-S6, Supporting Information). The TEM image also revealed the hollow mesoporous structure of the as-prepared HMONs. The hydrodynamic diameter of the as-prepared HMONs was ~ 64 nm based on the dynamic light scattering (DLS) analysis (Horiba SZ-100 (HORIBA, Ltd, Kyoto, Japan)) (Figure 1h). Meanwhile, HMONs displayed a typical type IV N_2 adsorption-desorption isotherms, confirming the mesoporous characteristics of the prepared HMONs (Figure S7a, Supporting Information). The Brunauer-Emmett-Teller (BET) surface area of HMONs was 424.8541 $m^2\ g^{-1}$. The pore size of HMONs peaked at 4.9 nm (Figure S7b, Supporting Information).

Next, "*in situ* polymerization" was introduced into the hollow cavity of HMONs. In brief, HMONs, mono-2-(methacryloyloxy)ethyl succinate and poly(ethylene glycol) methyl ether methacrylate were dispersed in anhydrous DMF. AIBN was used as a radical initiator to activate the polymerization (Scheme 1). After 1 h of the reaction, the polymerization was terminated by adding alcohol, followed by centrifugation and washing. Then, the resultant polymer was further modified with cysteamine *via* amidation reaction to achieve ample thiol groups in the cavity of HMONs. Despite the restriction of the shell of the HMONs, we also observed that after more than 2 h of polymerization, the polymers were extended to the outside of HMONs and formed a polymer shell on the HMONs (Figure 1d). Therefore, controlling the polymerization time is crucial to ensure the polymers growth within the cavity. As expected, without polymerization, the ultra-small Au NPs cannot be stably retained in the HMONs (Figure 1d). It was observed that with moderate polymerization, which was restricted within the hollow cavity, the ultra-small Au NPs were stably chelated within the hollow cavity of HMONs. After chelation, HMON-Au exhibited typical absorbance of Au NPs and HPPH in the UV-Vis spectrum (Figure 1a). Of note, with excessive polymerization to block the mesopores, the ultra-small Au NPs cannot enter the hollow cavity and the chelation was just restricted to the outer surface of HMONs (Figure 1d). The analysis of the size distribution based on the TEM images demonstrated that moderate polymerization did not substantially increase the size of the HMONs, while excessive polymerization significantly increased the size of the HMONs, further confirming the successful polymerization in HMONs (Figure S6b and S6c, Supporting Information).

Initially, we tested whether immobilizing the ultra-small Au NPs into HMONs could influence their catalysis capability. For the detection of H_2O_2 produced during the catalytic process, a hydrogen peroxide assay kit was employed in analysis. In the presence of horse radish peroxidase (HRP), the OxiRed probe reacts with H_2O_2 to produce product with color (λ_{max} = 570 nm). As shown in Figure 1e, after addition of ultra-small Au NPs, the reaction mixer turned to red, indicating the generation of H_2O_2. Immobilizing ultra-small Au NPs into HMONs slightly delayed the catalytic reaction, but did not ultimately interfere with the reaction (Figure 1e). Meanwhile, we observed that the generation of H_2O_2 largely depended on the concentration of glucose (Figure 1f). In the presence of HMON-Au, the catalytic reaction can rapidly reach the plateau, demonstrating the excellent catalytic efficiency of HMON-Au. Subsequently, TA was further deposited on the surface of HMON-Au and chelated Cu^{2+}. In our hypothesis, H_2O_2 will be converted to •OH in the presence of Cu-TA complexes through Fenton-like reaction. IR775, a radical scavenger, was used as a radical

indicator to determine the production of •OH.[17] Due to the interference of the UV-Vis absorbance of Au NPs, the catalytic efficiency of Cu-TA complexes was assessed in the acidic condition instead. As shown in Figure 1g, in the absence of Cu-TA complexes, H_2O_2 incubated with IR775 almost cannot produce any •OH. After addition of Cu-TA complexes into the solution, the absorbance of IR775 at 775 nm promptly decreased and finally reached the plateau over time, indicating the effective production of •OH. These results demonstrated that Cu-TA complexes can efficiently catalyze H_2O_2 into •OH in acidic condition. To further enhance the colloidal stability during systemic circulation *in vivo*, PVP was further coated onto the HMON-Au@Cu-TA to form HMON-Au@Cu-TA-PVP. After coating with PVP, the hydrodynamic diameter of nanoparticles slightly increased to ~ 102 nm (Figure 1h). As seen from the TEM image, a dense outer layer was coated onto the surface of HMONs (Figure S8, Supporting Information). Meanwhile, the coating layer substantially increased the colloidal stability of HMONs in phosphate buffer saline (PBS) solution, suggesting that HMON-Au@Cu-TA-PVP could be potentially used for biomedical application (Figure S9, Supporting Information). Taken together, these results demonstrated that the constructed HMON-Au@Cu-TA could efficiently catalyze the conversion of glucose into H_2O_2, which can be further converted into •OH through Fenton-like reaction.

2.2. Cellular uptake and intracellular ROS generation of HMON-Au@Cu-TA

Inspired by the above results, we next investigated the catalytic ability of HMON-Au@Cu-TA in BxPC-3 cells. Firstly, the cellular uptake efficiency of HMON-Au@Cu-TA was evaluated. BxPC-3 cells internalized large amounts of HMON-Au@Cu-TA nanoparticles (Figure S10 and S11, Supporting Information). The cellular uptake efficiency reached a plateau after 4 h of incubation. Then, the intracellular H_2O_2 generation was detected by a fluorescence peroxide probe. Since the Cu-TA complexes in HMON-Au@Cu-TA nanoparticles can convert H_2O_2 into •OH, thus interfering the detection of the generated H_2O_2, HMON-Au@PEG was used in this experiment instead. As displayed in Figure S12 (Supporting Information), the strong fluorescence signal was observed after HMON-Au@PEG treatment, indicating the immobilized ultra-small Au NPs maintained the catalytic capability in the intracellular environment as well.

Next, the intracellular ROS generation after treatment was detected using a ROS fluorescence probe 2′, 7′-dichlorofluorescein diacetate (DCFH-DA) as the indicator. Without laser irradiation (LI), HMON@Cu-TA cannot induce the generation of ROS in the presence or absence of glucose (Figure 2a and 2b), implying that endogenous H_2O_2 is not sufficient for Fenton-like reaction. While with LI, the cells incubated with HMON@Cu-TA showed strong fluorescence signal, further confirming that HPPH remained the photodynamic effect after hybridization within the framework of HMONs in the intracellular environment. We also observed that without LI, the cells treated with HMON-Au@Cu-TA also exhibited obvious fluorescence signal in the presence of glucose in the cell culture medium, implying the generation of large amount of intracellular ROS. In contrast, in the absence of glucose, there's almost no ROS generation after HMON-Au@Cu-TA treatment. As expected, the strongest fluorescence signal was observed in the cells treated with HMON-Au@Cu-TA with LI, probably resulted from the synergistic effect of PDT and CDT. The flow cytometric analysis revealed analogous results (Figure 2c-2e). These results

demonstrated that the integration of the GOx-like ultra-small Au NPs and Cu-TA can remarkably enhance the ROS generation in the intracellular environment, which can further increase intracellular ROS level after PDT.

To test whether the enhanced ROS generation can also improve the anti-cancer efficacy, the apoptosis effect in cells after treatment was examined. Without LI, HMON@Cu-TA led to negligible cytotoxicity in BxPC-3 cells, verifying the biocompatibility of HMONs (Figure 2f). With LI, large amounts of cells (~ 50%) underwent apoptosis after being treated with HMON@Cu-TA (Figure 2g). However, some cells still resisted to PDT, probably attributable to the limited ROS generation of PDT. Without LI, HMON-Au@Cu-TA treatment also led some cells (~ 30%) to undergo apoptosis in the presence of glucose, indicating CDT alone exhibited anti-cancer ability. Of note, the combination of PDT and CDT exhibited the most effective anti-cancer ability, almost all the tumor cells underwent apoptosis after HMON-Au@Cu-TA with LI treatment, further verifying the synergistic effect of PDT and CDT. Collectively, these results indicated that the generated ROS induced by CDT effect can enhance the anti-cancer effect of PDT *in vitro*.

2.3. Deep penetration of HMON-Au-Col@Cu-TA into 3D tumor spheroids

Since the ECM, especially the network of collagen, strongly hampered the penetration of nanoparticles,[18] Col, which can degrade collagen I fiber, was loaded into HMONs to enhance the penetration of nanoparticles and promote the O_2 infiltration. Three-dimensional (3D) tumor spheroids of BxPC-3 cells, mimicking the *in vivo* tumors, were constructed to investigate the tumor penetration of HMON-Au-Col@Cu-TA nanoparticles. As presented in Figure 3a, after introducing Col into HMONs, HMON-Au-Col@Cu-TA nanoparticles exhibited deep and strong penetration into 3D tumor spheroids, which can be visualized by the fluorescence signal of HPPH hybridized within the framework of HMONs. By contrast, the penetration of HMON-Au@Cu-TA nanoparticles into 3D tumor spheroids was just limited to the outer few cell layers of the spheroids. Subsequently, the cells in the 3D tumor spheroids were collected and subjected to flow cytometric analysis. The flow cytometric analysis indicated that ~ 70% of the cells in the 3D tumor spheroids took up HMON-Au-Col@Cu-TA nanoparticles (Figure 3b). This percentage was much higher than that after HMON-Au@Cu-TA (~ 30%) treatment, further indicating Col loaded in HMONs can enhance the nanoparticles penetration into 3D tumor spheroids. The analysis of the mean fluorescence intensity (MFI) of the collected cells from 3D tumor spheroids revealed that HMON-Au-Col@Cu-TA treatment led to a 4-fold increase in the MFI compared with HMON-Au@Cu-TA treatment (Figure 3c).

To test whether the enhanced penetration of HMON-Au-Col@Cu-TA nanoparticles was resulted from the Col mediated collagen I degradation, immunofluorescence examination was performed. It was observed that after HMON-Au-Col@Cu-TA treatment, the density of collagen in the 3D tumor spheroids was substantially decreased (Figure 3d). Meanwhile, we hypothesize that the degradation of the extracellular matrix may also promote O_2 infiltration, thus alleviating tumor hypoxia. Hypoxia-inducible factor 1α (HIF-1α), which is a major regulator of tumor cell adaptation to hypoxic stress, was used as an indicator of hypoxia of the 3D tumor spheroids. After indicated treatment, the 3D tumor spheroids were fixed and

stained with fluorophore-labeled antibodies against HIF-1α. Both the untreated and HMON-Au@Cu-TA treated 3D tumor spheroids exhibited strong fluorescence signals, confirming the hypoxia of 3D tumor spheroids (Figure 3e). However, after HMON-Au-Col@Cu-TA treatment, the hypoxia area was dramatically decreased compared to the untreated and HMON-Au@Cu-TA treatment, indicating reoxygenation capacity of HMON-Au-Col@Cu-TA. Flow cytometric analysis was further carried out to quantitatively evaluate the expression of HIF-1α. As shown in Figure 3f, the cells collected from 3D tumor spheroids treated with HMON-Au-Col@Cu-TA exhibited much lower HIF-1α expression than the untreated and HMON-Au@Cu-TA treatment group, consistent with the observation of confocal laser scanning microscopy (CLSM, Zeiss LSM 780 microscope) imaging. Together, these results demonstrated that HMON-Au-Col@Cu-TA can degrade the ECM, thereby enhancing the deep penetration of nanoparticles and promoting O_2 infiltration to alleviate hypoxia.

2.4. Enhanced tumor accumulation of HMON-Au-Col@Cu-TA-PVP

Encouraged by the above results, we next constructed a subcutaneous xenograft tumor model of pancreatic ductal adenocarcinoma in athymic nude mice to determine whether HMON-Au-Col@Cu-TA-PVP can also render enhanced accumulation of nanoparticles *in vivo*. First, the $^{64}Cu^{2+}$ was chelated into the nanocarrier to realize the positron emission tomography (PET) imaging. As displayed in Figure 4a, both HMON-Au@Cu-TA-PVP and HMON-Au-Col@Cu-TA-PVP nanoparticles began to accumulate in tumor tissues at 4 h after intravenous injection. The signal in tumor tissues peaked at 24 h after either HMON-Au@Cu-TA-PVP or HMON-Au-Col@Cu-TA-PVP injection. Interestingly, we observed that HMON-Au-Col@Cu-TA-PVP treatment rendered a significantly stronger signal in the tumor region over a long time (from 24 h to 48 h) compared with HMON-Au@Cu-TA-PVP treatment. The quantification of the signal intensity in tumor region demonstrated that the mice treated with HMON-Au@Cu-TA-PVP or HMON-Au-Col@Cu-TA-PVP showed almost equal signal intensity in the tumor regions from 1 h to 24 h, while the signal intensity of the tumor tissues after HMON-Au-Col@Cu-TA-PVP treatment began to exceed that after HMON-Au@Cu-TA-PVP treatment after 24 h of injection (Figure 4c and 4e), indicating that degradation of the ECM by the first arrived HMON-Au-Col@Cu-TA-PVP nanoparticles would be beneficial for the accumulation of subsequent nanoparticles into the tumor regions. Meanwhile, we also observed after peaking at 1h after injection, the liver uptake gradually decreased over time (Figure 4d).

With near-infrared fluorescence emission capability of HPPH hybridized HMONs, the tumor accumulation profiles after intravenous injection of nanoparticles were also tracked by fluorescence imaging. The fluorescence imaging showed similar results with PET imaging. Obvious fluorescence signals were observed in the tumor region of mice after either HMON-Au@Cu-TA-PVP or HMON-Au-Col@Cu-TA-PVP treatment (Figure 4b). The maximum tumor accumulation was achieved at 24 h after intravenous injection of HMON-Au-Col@Cu-TA-PVP. The mice after HMON-Au-Col@Cu-TA-PVP treatment exhibited stronger fluorescence signals in the tumor regions than those treated with HMON-Au@Cu-TA-PVP from 24 h to 48 h (Figure 4f). Moreover, after *in vivo* imaging, the tumor tissues were collected and subjected to frozen section. It was observed that large amounts of

HMON-Au-Col@Cu-TA-PVP nanoparticles accumulated and penetrated into the tumor tissues (Figure 4g). The fluorescence signal intensity of the tumor tissue after HMON-Au-Col@Cu-TA-PVP treatment was much higher than that after HMON-Au@Cu-TA-PVP treatment. These results further confirmed that the Col in the HMONs, in deed, enhance the accumulation and the penetration of nanoparticles into tumor tissues.

2.5. Anti-tumor efficacy of HMON-Au-Col@Cu-TA-PVP

Finally, the therapeutic efficacy of HMON-Au-Col@Cu-TA-PVP was evaluated in tumor xenografts of pancreatic ductal adenocarcinoma in *vivo*. LI alone didn't lead to any tumor growth inhibition or survival benefit (Figure 5a, 5b and Figure S13, Supporting Information). Without LI, HMON-Au@Cu-TA-PVP delayed the tumor growth to some extent, mainly resulted from CDT induced tumor cell apoptosis. In sharp contrast, with LI, HMON-Au@Cu-TA-PVP significantly inhibited the tumor growth, which could be ascribed to the synergistic anti-tumor effect of PDT and CDT. After introducing Col into HMONs, the anti-tumor efficacy was further enhanced. HMON-Au-Col@Cu-TA-PVP with LI treatment triggered prompt tumor regression and long-term, tumor-free survival in ~ 80% of the mice, superior to the other treatments. After treatment, the tumors were collected and subjected to immunofluorescence characterization. As displayed in Figure 5c, the tumor tissues of the mice treated with HMON-Au-Col@Cu-TA-PVP with LI showed decreased fluorescence signal intensity of collagen, confirming the degradation of ECM after treatment. Meanwhile, HMON-Au-Col@Cu-TA-PVP treatment also alleviated the hypoxia of the tumor tissues (Figure 5d and Figure S14, Supporting Information), confirming the degradation of ECM can promote the O_2 infiltration. Subsequently, the cell apoptosis in tumor tissues after treatment was also evaluated with terminal deoxynucleotidyl transferase deoxyuridine triphosphate (dUTP) nick end labeling (TUNEL) staining (Figure 5e). CDT alone induced some apoptotic cells in tumor tissues. Combination with PDT further enhanced the apoptosis-inducing effect. HMON-Au-Col@Cu-TA-PVP with LI treatment induced the strongest apoptosis in tumor cells consistent with the tumor growth inhibition efficiency. Additionally, all mice did not exhibit noticeable body-weight loss throughout the experimental period (Figure 5f). No sign of toxicity was observed throughout our studies. Histological analysis of the normal organs including heart, liver, spleen, lung, and kidney showed no evidence of abnormal and inflammatory cell infiltration in these organs after treatment (Figure S15, Supporting Information), indicating that treatment did not induce significant side effects in the mice.

3. Conclusion

In conclusion, we have developed a novel *in situ* polymerized hollow mesoporous organosilica biocatalysis nanoreactor for synergistic CDT/PDT. The photosensitizer for PDT was *in situ* hybridized within the framework of HMONs during preparation. The hollow cavity of HMONs was exploited as a nanoreactor for *in situ* polymerization of polymer containing thiol groups, which was further used to immobilize the GOx-like ultra-small Au NPs. In the study, Cu-TA complexes were then coated onto the surface of the HMONs *via* deposition effect. The ultra-small Au NPs catalyzed glucose into H_2O_2, which can be further converted into •OH by Fenton-like reaction *via* the catalysis of Cu-TA complexes. The

enhanced ROS generation after the combination of CDT and PDT led to effective anti-tumor therapeutic efficacy. Introducing Col into the nanoplatform enhanced tumor accumulation of nanoparticles and alleviated the hypoxia of the tumor tissues, thereby further enhancing the anti-tumor efficacy. To the best of our knowledge, this study is the first report that introduces *in situ* polymerization chemistry for grafting polymers into a hollow cavity to immobilize the nanozyme, which paves a new way for developing efficient combination strategy for enhancing ROS-mediated anti-tumor efficacy.

4. Experimental Section

Materials:

Hydrogen Peroxide Assay Kit, anti HIF-1α antibody and anti-collagen I antibody were purchased from Abcam. Annexin V/PI apoptosis detection kit was obtained from Biolegend. Fetal bovine serum (FBS), RPMI-1640, Penicillin-streptomycin and trypsin-EDTA were obtained from Gibco Life Technologies. Hoechst 33342 was provided by Thermal Fisher Scientific. HPPH was bought from MedKoo Biosciences, Inc. All other chemicals were bought from Sigma-Aldrich unless otherwise stated.

Preparation of HPPH hybridized HMONs:

In brief, HPPH was first conjugated with (3-aminopropyl)triethoxysilane (APTES) *via* amidation reaction. 10 g of CTAC solution and 0.5 g of TEA solution were mixed and 1 mL of TEOS was added to the solution. After 1 h of reaction, the mixtures of BTES and TEOS and HPPH-silane were added to the above mixture and reacted for another 4 h. Subsequently, the resultant HPPH-hybridized MSN@MON products were collected, washed with ethanol and dispersed in ddH_2O, followed by ammonia-assisted selective etching. The final HPPH-hybridized HMON products were obtained by centrifugation, washed and dispersed in ddH_2O.

Preparation of HMON-Au NPs:

Typically, HMONs (100 mg) and AIBN (5 mg, 0.02 mmol) were dissolved in 1 mL DMF solution in a 5 mL Schlenk tube. The mixture was added with freshly distilled mono-2-(Methacryloyloxy)ethyl succinate (203.73 mg, 0.88 mmol), Poly(ethylene glycol) methyl ether methacrylate (mPEGMA) (265 mg, 0.88 mmol). O_2 in the solution was degassed by argon blowing for 30 min. After vigorous stirring overnight at room temperature, the suspension was heated up to 65 °C and allowed to react for 1 h. The polymer containing silica was collected by precipitation in alcohol and centrifuged three times to completely remove the untrapped polymer. Noted that, when the polymerization time was extended to 2 h, the polymer grew outside HMONs. Then, the silica nanoparticles were dissolved in 5 mL DMF with appropriate EDC, NHS and excess cysteamine for overnight amidation reaction. The reaction solution was then centrifuged and washed by alcohol for three times. To prepare ultra-small Au NPs immobilized HMONs, the ultra-small Au NPs were first prepared according to the literature. The thiol based HMONs was dropped wisely into the concentrated ultra-small Au NPs solution under sonication. Followed by centrifugation, the dark red solid was obtained, donated as HMON-Au.

Preparation of HMON-Au-Col@Cu-TA-PVP:

In a typical procedure, 10 mg HMON-Au and 5 mg collagenase was dispersed in 0.5 mL of distilled water, followed by the addition of 25 μL of tannic acid solution (40 mg mL^{-1}).The mixture solution was under sonication for 10 min. Then, 50 μL of $CuCl_2$ solution (10 mg mL^{-1}) was added to the suspension. HEPES buffer (pH = 7.4) was added into the solution stirred for 2 h to initiated the coordination reaction between Cu^{2+} and tannic acid. Finally, the HMON-Au-Col@Cu-TA was obtained by centrifugation. Due to the hydrogen bonding between PVP and tannic acid, the PVP can coat HMON-Au-Col@Cu-TA. For PVP coating, the HMON-Au@Cu-TA was added dropwisely into PVP solution (10 mg mL^{-1}) under sonication and the HMON-Au-Col@Cu-TA-PVP was obtained by centrifugation and washing.

Cell culture:

BxPC-3 cells (human pancreas cancer cells), were purchased from ATCC (USA). Cells were cultured in RPMI-1640 medium supplemented with 10% FBS and 0.1% penicillin-streptomycin at 37 °C, in a humidified 5% CO_2 atmosphere.

Cell uptake analysis:

In this study, BxPC-3 cells were seeded into 12-well plate (1.0×10^5 cells per well) and cultured overnight. HMON-Au@Cu-TA were added to the wells and incubated at 37 °C. After 0.5, 1, 2, and 4 h of incubation, the cells were harvested, rinsed with cold PBS, re-suspended in PBS for the flow cytometric analysis or stained with Hoechst 33342 and subjected to confocal fluorescence microscopy (CLSM) (ZEISS, LSM 780, Germany) imaging.

Intracellular ROS generation analysis:

BxPC-3 cells were seeded into 12-well plate (1.0×10^5 cells per well) and cultured overnight. Then, the medium was replaced with fresh medium without glucose or fresh medium with glucose and cultured for another 6 h. Then HMON@Cu-TA or HMON-Au@Cu-TA nanoparticles were added to the medium and incubated with cells for 4 h. Then the cells were incubated with DCFH-DA (10 μM) for 30 min. For laser irradiation treatment, the cells were washed with PBS and exposed to a 671 nm laser (0.1 W cm^{-2}) for 10 min and observed with CLSM.

Penetration into 3D Tumor Spheroids:

The 3D tumor spheroids of BxPC-3 were established. Briefly, BxPC-3 cells (5×10^3 per well) were plated in 96-well plates precoated with low melting point agarose. After 5 days of incubation, the 3D tumor spheroids were collected and treated with HMON-Au@Cu-TA or HMON-Au-Col@Cu-TA for 16 h. Then, tumor spheroids were washed and fixed, followed by CLSM observation. For immunofluorescence staining of HIF-1α, the fixed tumor spheroids were treated with 0.5% Triton X-100 for 30 min, blocked and stained with antibody against HIF-1α (dilution 1:200).

In vivo imaging analysis:

All animal experiments were carried out in accordance with the Guide Protocol of Laboratory Animals, approved by the Ethics Committee of National Institutes of Health (NIH, USA). The subcutaneous xenograft pancreatic ductal adenocarcinoma tumor model was established by subcutaneous injection of BxPC-3 cells (5×10^6 cells for each mouse) in the flank of the athymic nude mice. The tumor size was monitored and the tumor volume (V) was calculated as $V=L\times W^2/2$, where L and W indicated the length and width of the tumor, respectively. At day 18 post inoculation, 100 μL of HMON-Au@^{64}Cu-TA-PVP or HMON-Au-Col@^{64}Cu-TA-PVP nanoparticles were intravenously injected. Then, PET imaging was performed at the determined time point. After completion of the PET imaging, the mice were sacrificed. The tumors and major organs including heart, liver, spleen, lung, and kidney were collected for quantification. For fluorescence imaging, 100 μL of HMON-Au@Cu-TA-PVP or HMON-Au-Col@Cu-TA-PVP nanoparticles were intravenously injected.

In vivo Tumor Inhibition Study:

The subcutaneous pancreatic ductal adenocarcinoma model was established as previously described. When the tumor volumes reached ~ 100 mm^3 after cell inoculation, the indicated nanoparticles were intravenously injected. 24 h after injection, the corresponding tumors were subjected to 671 nm laser irradiation (0.2 W cm^{-2}, 10 min). The tumor volumes and body weights of mice were monitored every three days. At the end of the experiment, mice were euthanized. The tumors as well as the major organs were collected, photographed, weighed, and then fixed in 4% paraformaldehyde for hematoxylin and eosin (H&E) staining and immunofluorescence characterization analysis.

Statistical Analysis:

Data were presented as mean± s.d. Significant differences between groups were indicated by $*P < 0.05$, $**P < 0.01$, $***P < 0.001$, $****P < 0.0001$, respectively.

Supplementary Material

Refer to Web version on PubMed Central for supplementary material.

Acknowledgements

This work was supported by the Intramural Research Program of the National Institute of Biomedical Imaging and Bioengineering (NIBIB), National Institutes of Health (NIH), the National Natural Science Foundation of China (Nos. 91859207, 81771873, and 81471689).

References

[1]. a)Chen H, Qiu Y, Ding D, Lin H, Sun W, Wang GD, Huang W, Zhang W, Lee D, Liu G, Adv. Mater 2018, 30, 1802748;b)Fan W, Huang P, Chen X, Chem. Soc. Rev 2016, 45, 6488; [PubMed: 27722560] c)Wang H, Chao Y, Liu J, Zhu W, Wang G, Xu L, Liu Z, Biomaterials 2018, 181, 310; [PubMed: 30096565] d)Choi JR, Yong KW, Choi JY, Nilghaz A, Lin Y, Xu J, Lu X, Theranostics 2018, 8, 1005; [PubMed: 29463996] e)Dong Z, Feng L, Hao Y, Chen M, Gao M, Chao Y, Zhao H, Zhu W, Liu J, Liang C, Zhang Q, Liu Z, J. Am. Chem. Soc 2018, 140, 2165. [PubMed: 29376345]

[2]. a)Zhou Z, Song J, Nie L, Chen X, Chem. Soc. Rev 2016, 45, 6597; [PubMed: 27722328] b)Liu C, Wang D, Zhang S, Cheng Y, Yang F, Xing Y, Xu T, Dong H, Zhang X, ACS Nano 2019, 13, 4267; [PubMed: 30901515] c)Zhu T, Shi L, Yu C, Dong Y, Qiu F, Shen L, Qian Q, Zhou G, Zhu X, Theranostics 2019, 9, 3293. [PubMed: 31244955]

[3]. Gad H, Koolmeister T, Jemth A-S, Eshtad S, Jacques SA, Strom CE, Svensson LM, Schultz N, Lundback T, Einarsdottir BO, Nature 2017, 544, 508. [PubMed: 28447629]

[4]. a)Lin L, Huang T, Song J, Ou X-Y, Wang Z, Deng H, Tian R, Liu Y, Wang J-F, Liu Y, J. Am. Chem. Soc 2019, 141, 9937; [PubMed: 31199131] b)Fan JX, Peng MY, Wang H, Zheng HR, Liu ZL, Li CX, Wang XN, Liu XH, Cheng SX, Zhang XZ, Adv. Mater 2019, 31, 1808278.

[5]. a)Tang Z, Liu Y, He M, Bu W, Angew. Chem. Int. Ed 2019, 58, 946;b)Ranji-Burachaloo H, Gurr PA, Dunstan DE, Qiao GG, ACS Nano 2018, 12, 11819. [PubMed: 30457834]

[6]. a)Tang Z, Zhang H, Liu Y, Ni D, Zhang H, Zhang J, Yao Z, He M, Shi J, Bu W, Adv. Mater 2017, 29, 1701683;b)Zhang L, Wan S-S, Li C-X, Xu L, Cheng H, Zhang X-Z, Nano Lett. 2018, 18, 7609. [PubMed: 30383966]

[7]. a)Jiang D, Ni D, Rosenkrans ZT, Huang P, Yan X, Cai W, Chem. Soc. Rev 2019, 48, 3683; [PubMed: 31119258] b)Shi S, Wu S, Shen Y, Zhang S, Xiao Y, He X, Gong J, Farnell Y, Tang Y, Huang Y, Gao L, Theranostics 2018, 8, 6149. [PubMed: 30613289]

[8]. a)Huang Y, Ren J, Qu X, Chem. Rev 2019, 119, 4357; [PubMed: 30801188] b)Zhang A, Pan S, Zhang Y, Chang J, Cheng J, Huang Z, Li T, Zhang C, de la Fuentea JM, Zhang Q, Cui D, Theranostics 2019, 9, 3443; [PubMed: 31281489] c)Wu J, Wang X, Wang Q, Lou Z, Li S, Zhu Y, Qin L, Wei H, Chem. Soc. Rev 2019, 48, 1004. [PubMed: 30534770]

[9]. a)Luo W, Zhu C, Su S, Li D, He Y, Huang Q, Fan C, ACS Nano 2010, 4, 7451; [PubMed: 21128689] b)Huang Y, Zhao M, Han S, Lai Z, Yang J, Tan C, Ma Q, Lu Q, Chen J, Zhang X, Adv. Mater 2017, 29, 1700102.

[10]. a)Choi HS, Liu W, Misra P, Tanaka E, Zimmer JP, Ipe BI, Bawendi MG, Frangioni JV, Nat. Biotechnol 2007, 25, 1165; [PubMed: 17891134] b)Choi HS, Liu W, Liu F, Nasr K, Misra P, Bawendi MG, Frangioni JV, Nat. Nanotechnol 2010, 5, 42. [PubMed: 19893516]

[11]. a)Wu M, Meng Q, Chen Y, Zhang L, Li M, Cai X, Li Y, Yu P, Zhang L, Shi J, A Adv. Mater 2016, 28, 1963; [PubMed: 26743228] b)Cheng CA, Deng T, Lin FC, Cai Y, Zink JI, Theranostics 2019, 9, 334;c)Chen Y, Shi J, Adv. Mater 2016, 28, 3235; [PubMed: 26936391] d)Chen Y, Meng Q, Wu M, Wang S, Xu P, Chen H, Li Y, Zhang L, Wang L, Shi J, J. Am. Chem. Soc 2014, 136, 16326. [PubMed: 25343459]

[12]. Liu T, Zhang M, Liu W, Zeng X, Song X, Yang X, Zhang X, Feng J, ACS Nano 2018, 12, 3917. [PubMed: 29578680]

[13]. a)Guo J, Ping Y, Ejima H, Alt K, Meissner M, Richardson JJ, Yan Y, Peter K, Von Elverfeldt D, Hagemeyer CE, Angew. Chem. Int. Ed 2014, 53, 5546;b)Ejima H, Richardson JJ, Liang K, Best JP, van Koeverden MP, Such GK, Cui J, Caruso F, Science 2013, 341, 154. [PubMed: 23846899]

[14]. Yao X, Zheng X, Zhang J, Cai K, RSC Adv. 2016, 6, 76473.

[15]. a)Bellnier DA, Greco WR, Loewen GM, Nava H, Oseroff AR, Pandey RK, Tsuchida T, Dougherty TJ, Cancer Res. 2003, 63, 1806; [PubMed: 12702566] b)Liu Z, Wang Q, Fan L, Wu DP, Zhang Y, Liu L, Tao L, Lasers Surg. Med 2015, 47, 68. [PubMed: 25483871]

[16]. Feng L, Li H, Qu Y, Lü C, Chem. Commun 2012, 48, 4633.

[17]. Yang Z, Dai Y, Yin C, Fan Q, Zhang W, Song J, Yu G, Tang W, Fan W, Yung BC, Li J, Li X, Li X, Tang Y, Huang W, Song J, Chen X, Adv. Mater 2018, 30, 1707509.

[18]. a)Provenzano PP, Eliceiri KW, Campbell JM, Inman DR, White JG, Keely PJ, BMC Med. 2006, 4, 38; [PubMed: 17190588] b)Netti PA, Berk DA, Swartz MA, Grodzinsky AJ, Jain RK, Cancer Res. 2000, 60, 2497. [PubMed: 10811131]

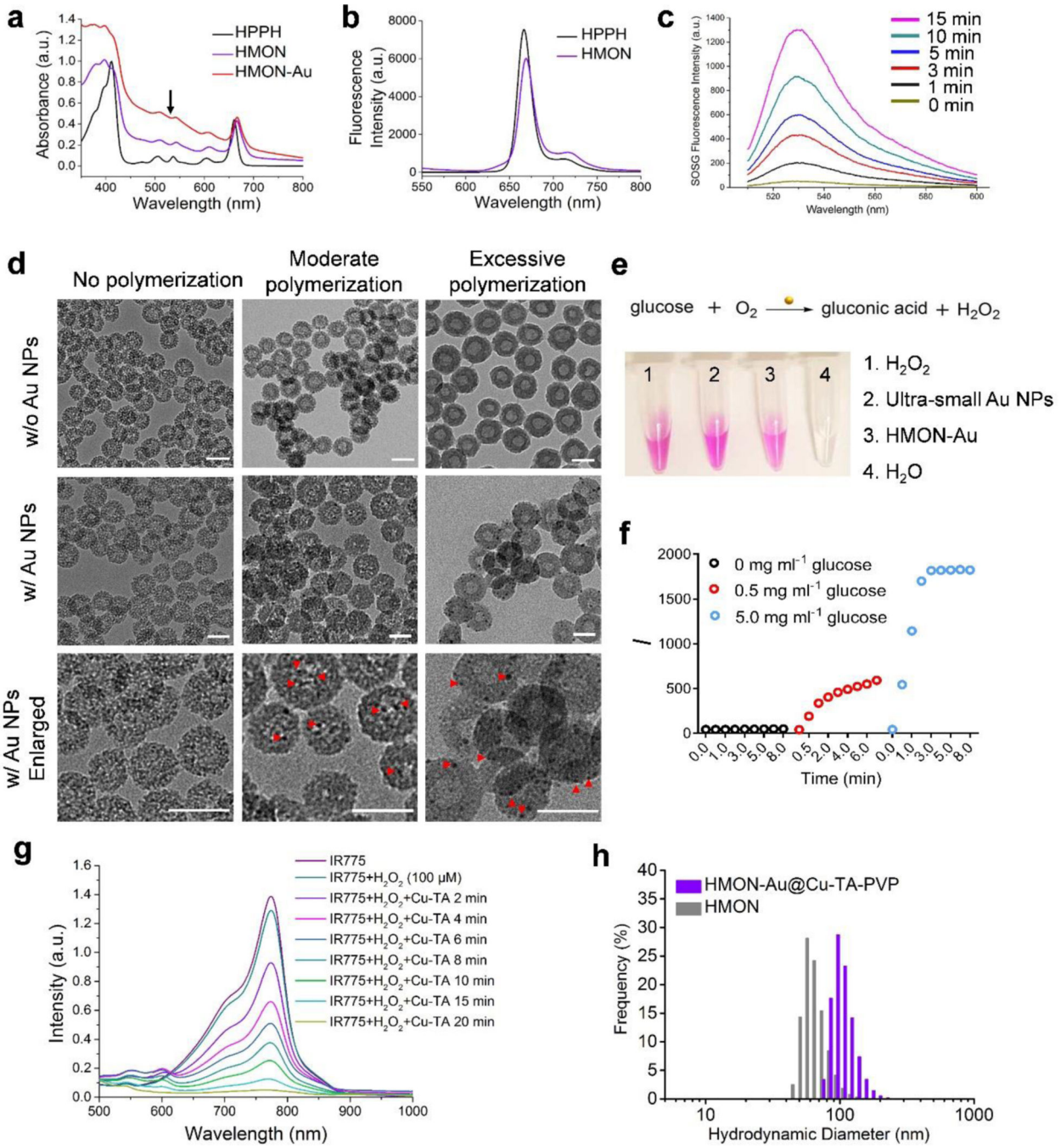

Figure 1.

Preparation and characterization of HPPH hybridized HMONs (abbreviated as “HMON”), HMONs immobilized with the ultra-small Au NPs (HMON-Au) and HMON-Au@Cu-TA-PVP nanoparticles. (a) UV-Vis absorption of HPPH, HMON and HMON-Au. (b) Fluorescence spectra of HPPH and HMON. (c) Fluorescence spectra of the SOSG solution incubated with HMON over increased irradiation time. (d) Morphologies of HMON with no polymerization, HMON with moderate polymerization, and HMON with excessive polymerization (the upper panel, w/o Au NPs) detected by TEM; morphologies of HMON

with no polymerization, HMON with moderate polymerization, and HMON with excessive polymerization incubated with the ultra-small Au NPs (the middle and lower panel, w/ Au NPs) detected by TEM. Scale bar, 50 nm. (e) The digital images of H_2O_2 production after indicated treatment detected by Hydrogen Peroxide Assay Kit. (f) The quantification of H_2O_2 production in the presence of HMON-Au at indicated concentration of glucose. (g) UV-Vis absorption of IR775, a radical indicator, after indicated treatment. (h) Size distribution of HMON and HMON-Au@Cu-TA-PVP nanoparticles measured by DLS.

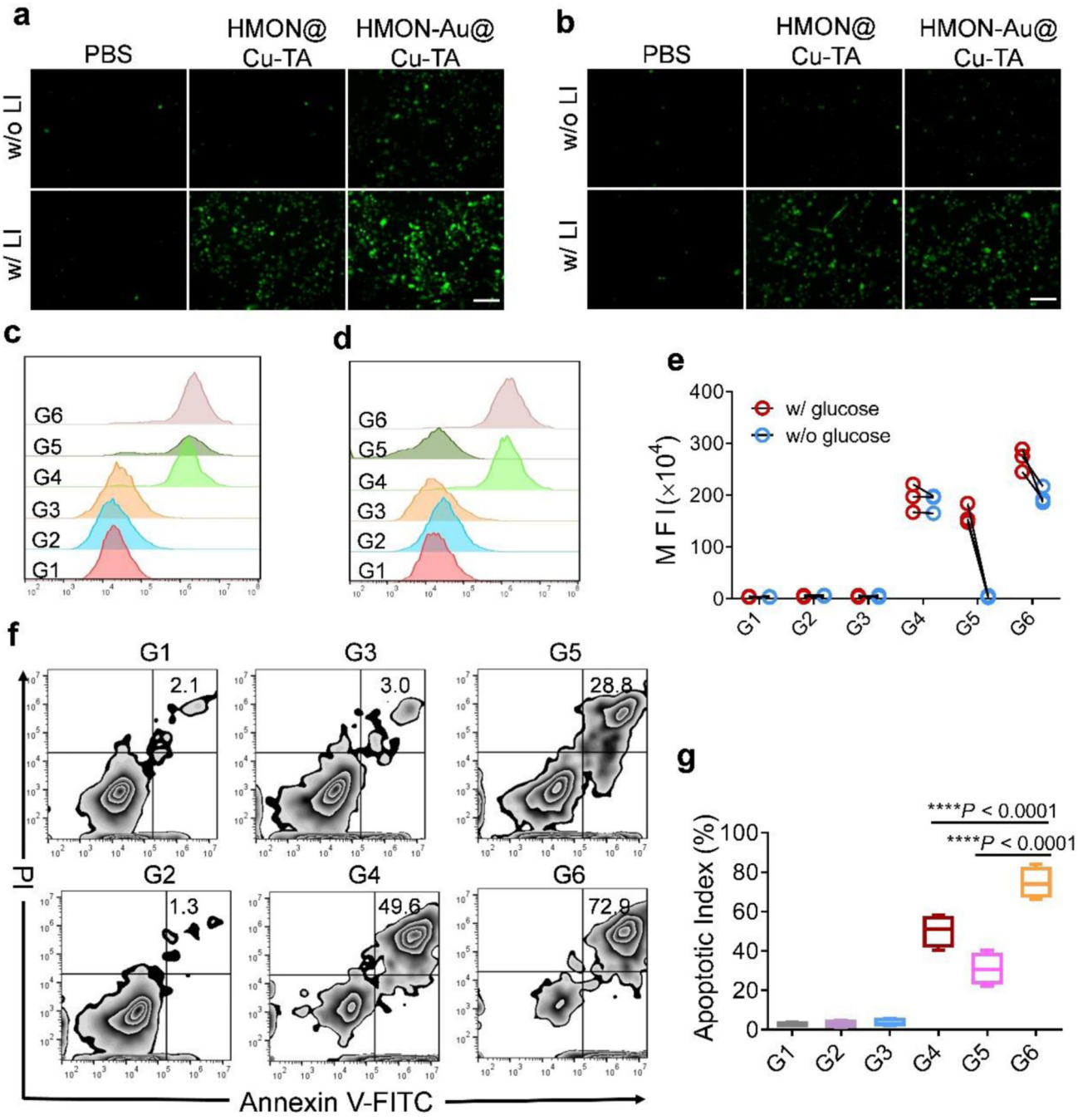

Figure 2.

(a-e) The detection of intracellular ROS generation after treatment using a ROS fluorescence probe DCFH-DA as the indicator. Fluorescence images (a) and flow cytometric analysis (c) of ROS generation in BxPC-3 cells after indicated treatment in the culture medium with glucose. Fluorescence images (b) and flow cytometric analysis (d) of ROS generation in BxPC-3 cells after indicated treatment in the culture medium without glucose. (e) The quantification of mean fluorescence intensity (MFI) in BxPC-3 cells after indicated treatment. (f) Flow cytometric analysis of apoptosis in BxPC-3 cells after indicated

treatment. (g) The quantification of apoptotic index in BxPC-3 cells after indicated treatment. Scale bar, 100 μm. G1, PBS without LI; G2, PBS with LI; G3, HMON@Cu-TA without LI; G4, HMON@Cu-TA with LI; G5, HMON-Au@Cu-TA without LI; G6, HMON-Au@Cu-TA with LI. Data are presented as means ± s.d. Statistical significance was calculated *via* one-way ANOVA with Tukey post-hoc test (g).* $P < 0.05$, ** $P < 0.01$, *** $P < 0.001$, **** $P < 0.0001$.

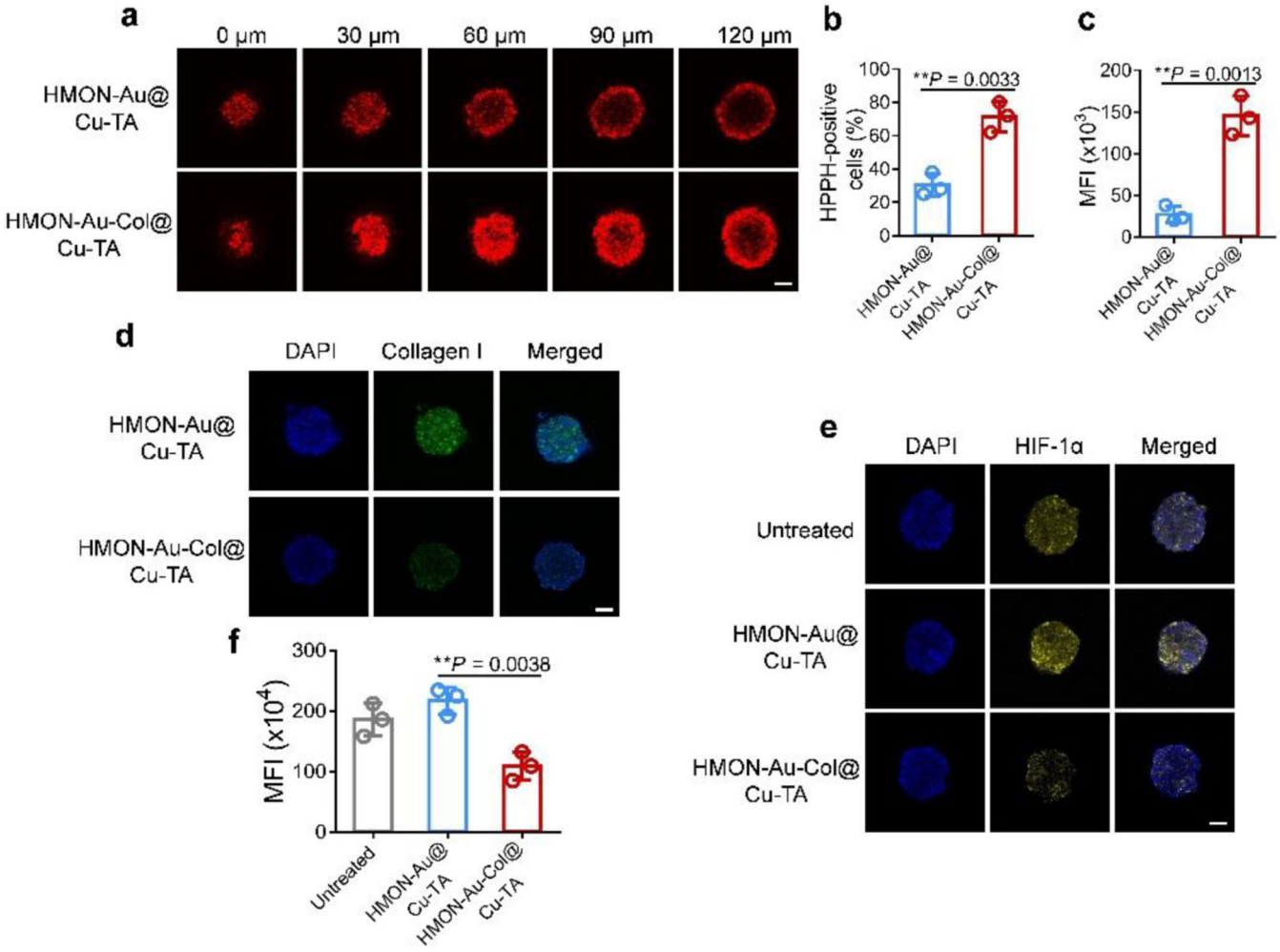

Figure 3.

(a) Penetration ability of HMON-Au@Cu-TA and HMON-Au-Col@Cu-TA into 3D tumor spheroids of BxPC-3 cells. (b, c) The quantification of the percentage (b) and MFI (c) of HPPH positive cells in the 3D tumor spheroids. (d) The immunofluorescence characterization of the collagen I fiber in the 3D tumor spheroids after indicated treatment. (e) The hypoxia evaluation of 3D tumor spheroids after various treatments. Hypoxia was assessed by staining with HIF-1α (green). (f) The quantification of HIF-1α expression in 3D tumor spheroids after various treatments by flow cytometric analysis. Scale bar, 100 μm. Data are presented as means ± s.d. Statistical significance was calculated *via* two-tailed Student's *t*-test (b, c) or one-way ANOVA with Tukey post-hoc test (f).* $P < 0.05$, ** $P < 0.01$, *** $P < 0.001$, **** $P < 0.0001$.

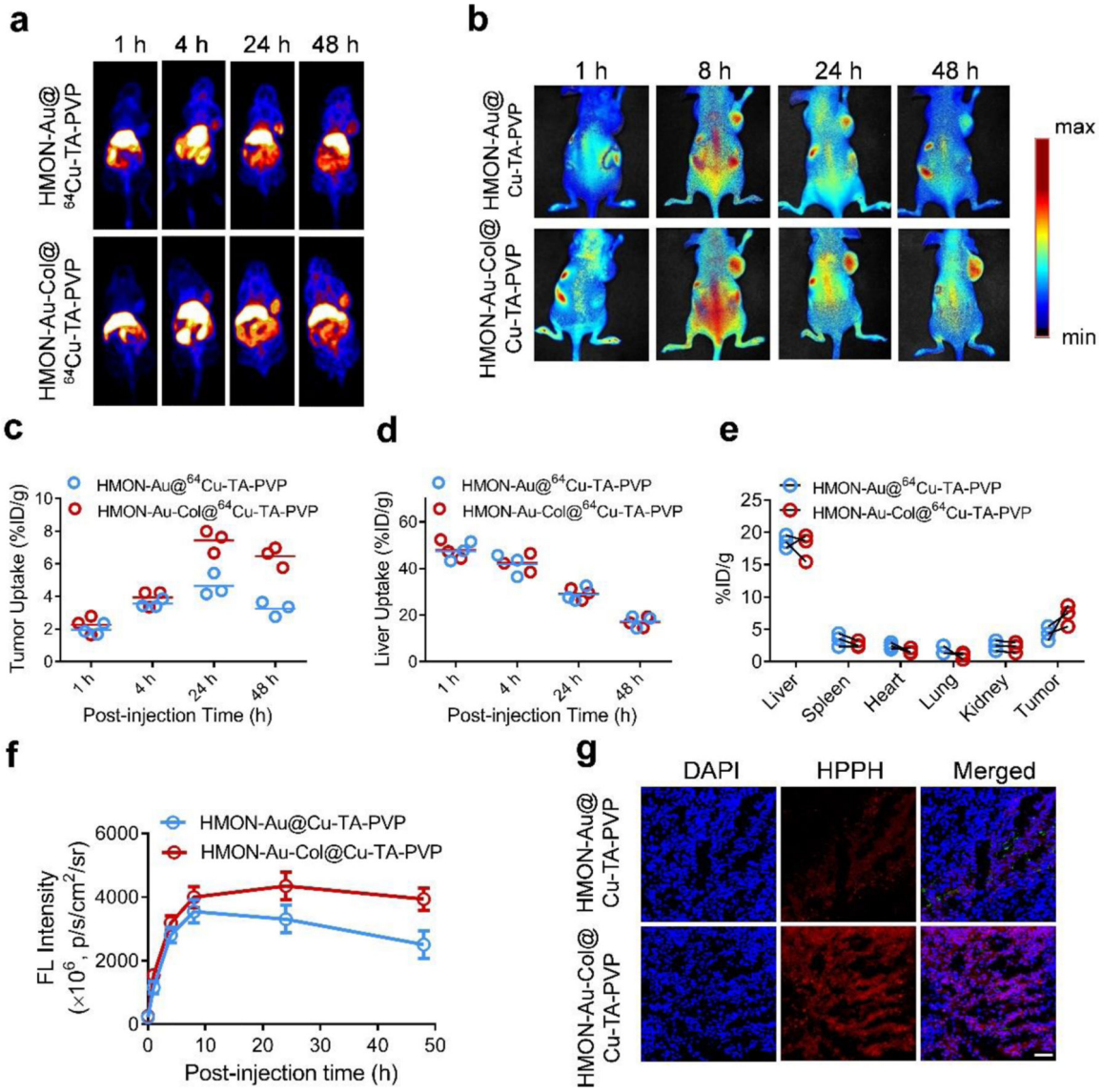

Figure 4.

In vivo distribution of HMON-Au@Cu-TA-PVP and HMON-Au-Col@Cu-TA-PVP nanoparticles in tumor-bearing mice. (a) Representative *in vivo* images of tumor-bearing mice at designated time point after intravenous injection with indicated formulation detected by PET imaging. (b) Representative *in vivo* fluorescence images of tumor-bearing mice after intravenous injection with indicated formulation. (c, d) The quantification of tumor uptake (c) and liver uptake (d) of HMON-Au@^{64}Cu-TA-PVP or HMON-Au-Col@^{64}Cu-TA-PVP nanoparticles over time by PET scanning at 1, 4, 24, and 48 h post injection. (n = 3/group) (e) The quantification of the PET signal intensity in the main organs of tumor-bearing mice at 48 h post injection. (f) The quantification of the fluorescence signal intensity in tumor at designated time point after indicated treatment. (g) Representative confocal laser scanning microscopy (CLSM) images of the tumor frozen section after indicated treatment. Scale bar, 100 μm.

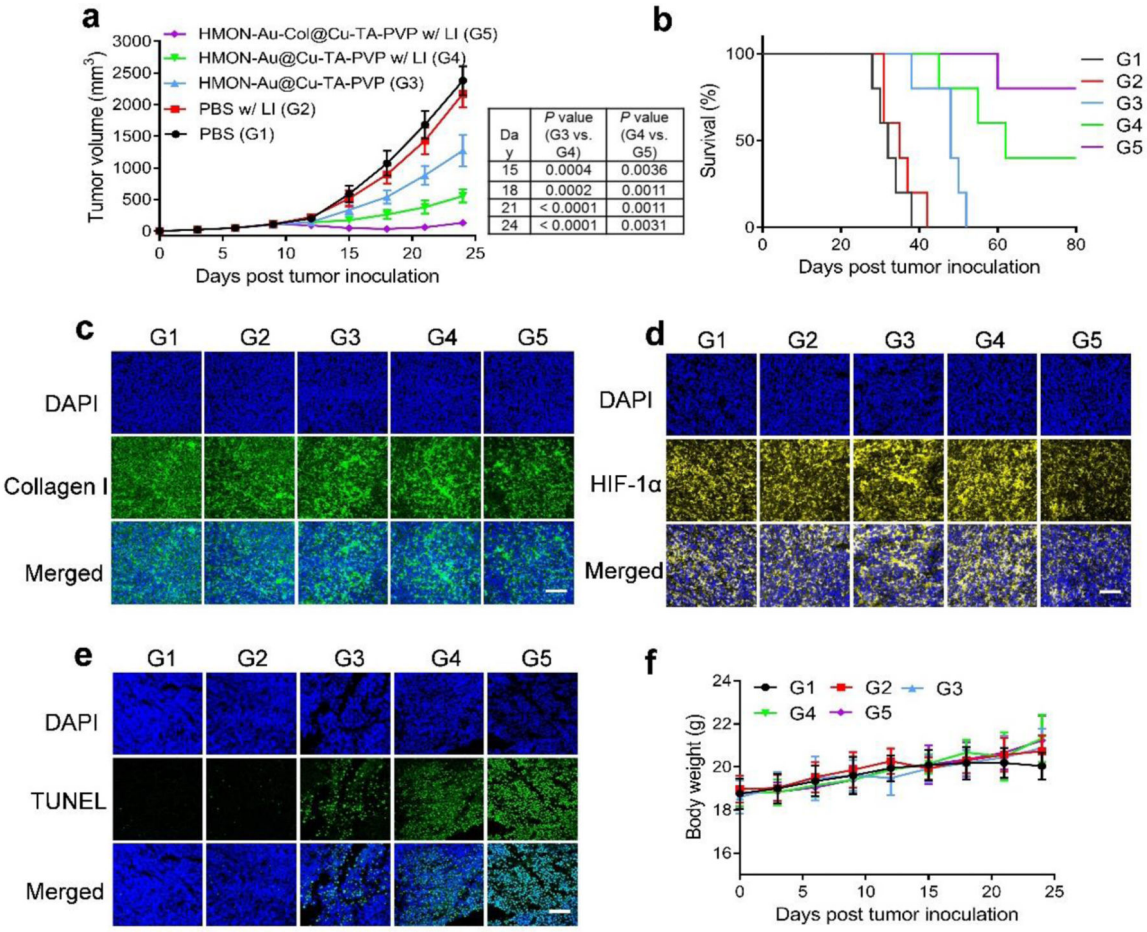

Figure 5.

The anti-tumor efficacy of synergistic PDT and CDT. (a) The average tumor growth curves after treatment. (b) Survival curves after treatment. (c-e) Immunofluorescence characterization of the collagen I fiber (c), HIF-1α (d) and TUNEL (e) in the tumor sections after treatment. (f) The body weight variation of tumor-bearing mice during treatment. Scale bar, 100 μm. G1, PBS; G2, PBS with LI; G3, HMON-Au@Cu-TA-PVP; G4, HMON-Au@Cu-TA-PVP with LI; G5, HMON-Au-Col@Cu-TA-PVP with LI. Data are presented as means ± s.d. Statistical significance was calculated *via* one-way ANOVA with Tukey post-hoc test (a).* $P < 0.05$, ** $P < 0.01$, *** $P < 0.001$, **** $P < 0.0001$.

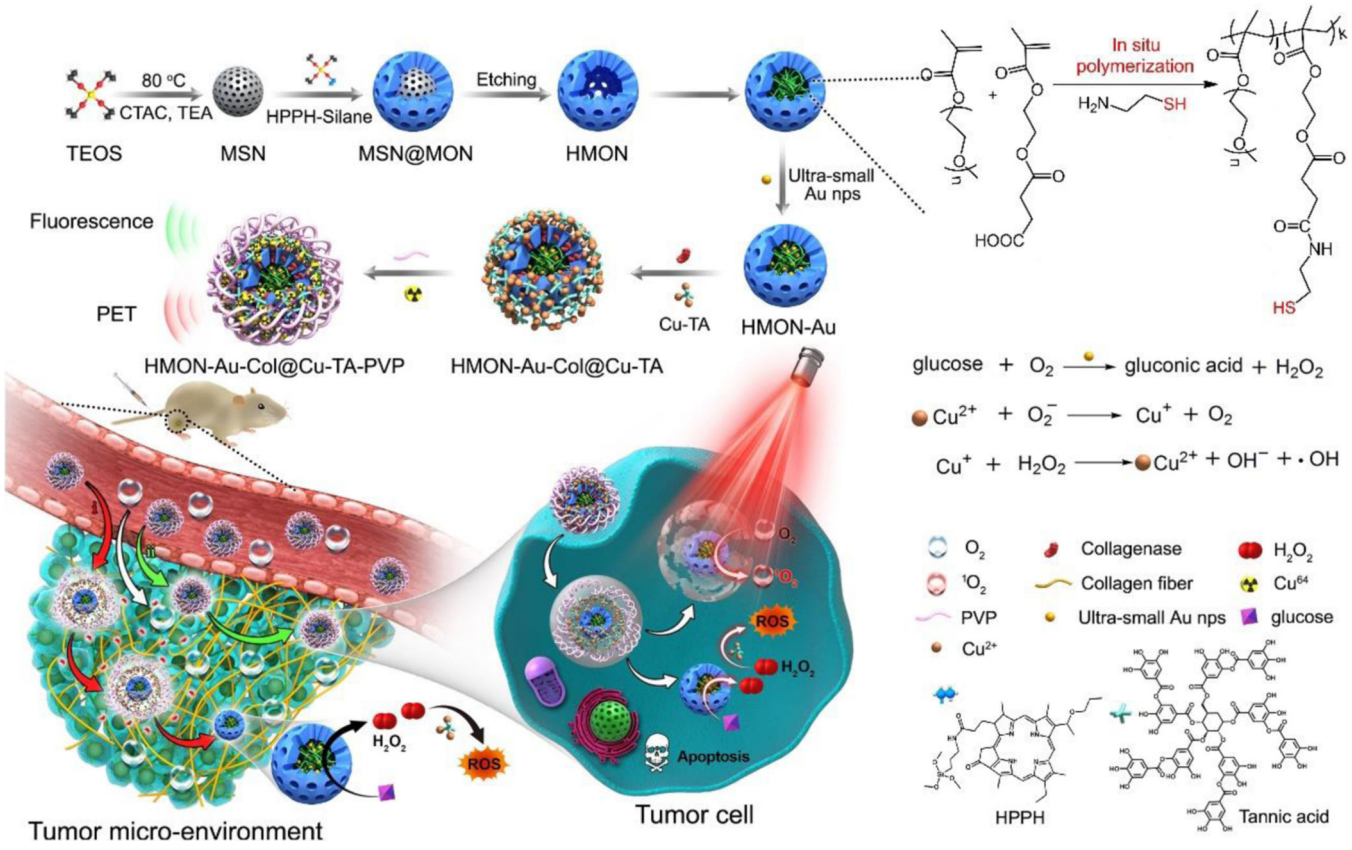

Scheme 1.

Schematic showing the process of preparing *in situ* polymerized hollow mesoporous organosilica biocatalysis nanoreactor for synergistic photodynamic (PDT)/chemodynamic (CDT) therapy.